Supporting Information

Weber and Deutsch 10.1073/pnas.1317193111

Materials and Methods

1. Ocean Model. ***Ocean circulation model.*** We used an Ocean General Circulation Model in which circulation is constrained to simultaneously satisfy both large-scale dynamical balances and hydrographic tracer observations (temperature, salinity, and ^{14}C) (1). It has horizontal resolution of 4° × 4°, and 24 vertical layers including 2 in the top 75 m. Annual mean flow fields are extracted as a matrix (**A**), and biogeochemical simulations performed using the Transport Matrix Method (2).

Ecosystem model. We used the simple ecosystem model described by ref. 3, which simulates the cycles of PO_4 (P) and NO_3 (N), including dissolved organic matter dynamics, and contains "general" phytoplankton (O) and N_2-fixing diazotropic phytoplankton (F) that compete for resources. Modifications are described here, and new parameters are listed in Table S1. The primary extension for this study is the addition of a prognostic Fe cycle (see below), in which Fe becomes a potentially limiting resource for plankton growth. The growth and mortality of the two plankton groups are thus governed by:

$$\frac{dO}{dt} = \mu_o \min\left(\frac{\mathrm{P}}{\mathrm{P}+K_P}, \frac{\mathrm{N}}{\mathrm{N}+K_N}, \frac{\mathrm{Fe}}{\mathrm{Fe}+K_{Fe}}\right) O - MO \qquad \textbf{[S1]}$$

$$\frac{dF}{dt} = \mu_F \min\left(\frac{\mathrm{P}}{\mathrm{P}+K_P}, \frac{\mathrm{Fe}}{\mathrm{Fe}+K_{Fe}}\right) F - MF. \qquad \textbf{[S2]}$$

Here, μ_o and μ_F are the maximum growth rates of O and F, respectively, as a function of ambient temperature and light conditions, and M represents phytoplankton mortality, including a quadratic term that scales with total biomass ($M = m_1 + m_2B$, where $B = O + F$ and m_1 and m_2 are constants). Although this model lacks a representation of higher trophic levels, it was shown to accurately reproduce observed nutrient distributions and the broad biogeography of diazotrophic plankton, which are confined to warm oligotrophic subtropical gyre regions (4). All model runs are integrated to a steady state, defined as an N budget imbalance of <1 TgN/y, which generally requires 5–10 thousand model years.

Denitrification. To use tracer distributions to constrain the Fe limitation of N_2 fixation, we must ensure that other processes affecting these tracers are accurately represented. The most important of these processes is denitrification. As in ref. 3, we impose the pattern and rate of water-column denitrification derived from inverse model estimates of N losses (5) (Fig. S1), with the eastern tropical North and South Pacific suboxic zones each contributing 25 TgN loss per year, and the Arabian Sea contributing 15 TgN/y (Fig. S1*A*). The distribution of benthic denitrification is governed by the flux of organic matter to the seafloor (6), but rates are scaled to meet a specified global total (Fig. S1*B*). Because the global benthic flux is less well constrained, we conduct four simulations for each Fe limitation scenario (i.e., each value of Q_F/Q_O), with total sediment N losses of 100, 140, 180 and 220 TgN/y, bracketing the range estimated from observations (7). Model results are presented as the average of this model ensemble, with intermodel SD taken as an uncertainty estimate.

Fe cycle. We used the Fe cycle model of ref. 8, with minimal modifications. Briefly, Fe is supplied to the surface ocean from an aeolean source based on dust fluxes from an atmospheric transport model (9). Dissolved Fe bonds with organic ligands through complexation reactions that occur on short timescales (minutes to hours) and are thus assumed to go to equilibrium. Free (unbound) Fe is removed from the ocean via scavenging, following a first-order relation. All parameters governing dissolution, complexation, and scavenging, as well as the Fe:P ratio of "regular" (nondiazotrophic) organic matter (Q_O in our model), are taken from refs. 8 and 10 (Table S1). Simulated Fe fields are similar to ref. 8, and capture the observed large-scale patterns in surface and intermediate-water dissolved Fe (Fig. S2).

O_2 cycle. We performed a set of additional simulations to investigate the effect of N_2 fixation on the rates of denitrification between the Pacific and Indian oceans. In these model runs, the data-derived rates of water-column denitrification were replaced by a prognostic representation, necessitating the simulation of dissolved oxygen (O_2). The O_2 cycle is simulated following standard Ocean Carbon Model Intercomparison Project protocol:

$$\frac{d\mathrm{O}_2}{dt} = A\mathrm{O}_2 + K_W\left(\mathrm{O}_{2,sat} - \mathrm{O}_2\right) + r_{O:N} J_{bio,N}.$$

Here, A is the transport operator, K_W is the piston velocity for O_2 gas exchange, $O_{2,sat}$ is the saturation O_2 concentration, $J_{bio,N}$ is the sum of biological production and remineralization N fluxes, and $r_{O:N}$ is the ratio of oxygen production (or removal) to nitrate uptake (release) during organic matter production (remineralization). When the oxidant demands of remineralization would draw O_2 below zero, O_2 consumption is prevented and the residual oxidant demand is met through denitrification with the known stoichiometry of the net reaction, r_{den} = N loss/N remineralization = 104/16 (11).

To improve the representation of suboxic zones, simulations with the explicit O_2 cycle are conducted in a 2° × 2° configuration of the observationally constrained circulation model (5). Uncertainty estimates were derived by using two different transport operators, one of which employs an additional chlorofluorocarbon 11 (CFC-11) constraint, and by repeating our experiments with a longer dissolved organic matter (DOM) turnover timescale (Table S1).

^{15}N cycle. In addition to nutrient concentrations, we simulated the isotopic distribution of NO_3 following the procedure described in ref. 7. Briefly, each steady-state flux of N (J_N, including biological uptake, reminearlization, N_2 fixation, and benthic and water-column denitrification) is converted into a ^{15}N flux using a fractionation factor α:

$$J_{^{15}N} = \alpha \frac{^{15}\mathrm{N}}{^{14}\mathrm{N}} J_N.$$

The governing equations for $^{15}NO_3$ and ^{15}DON are then cast in terms of the isotopic ratio $R = {}^{15}\mathrm{N}/{}^{14}\mathrm{N}$ producing a linear system that can be solved directly by matrix inversion for the steady state. These ratios are then converted into $\delta^{15}N$ values for comparison with observations, which are usually reported in this notation. See Table S1 for enrichment factors (ε) factors, which are related to fractionation factors by $\varepsilon = (1 - \alpha)*1000$.

Fe fertilization. We conducted two sets of simulations in which the atmospheric Fe supply to the ocean was manipulated to test the degree of Fe limitation in diazotroph communities and their response to different dust deposition regimes. Each experiment was initialized with the steady-state solution that fit our observational constraints (Fig. 2) best, in which $Q_F/Q_O = 20$.

First, to test whether N_2 fixation is Fe-limited at the basin-scale, the Fe supply across the entire Pacific was enhanced by 1 gFe m^{-2} y^{-1}, and the model was integrated for 200 y.

Denitrification was held at specified rates to isolate the response of N_2 fixation to the alleviation of Fe limitation, rather than the response to changing N deficits. Second, to test the long-term sensitivity of marine N_2 fixation and the ocean's N reservoir to climate-driven changes in the dust supply, we scaled the model Fe deposition fluxes globally by a factor ranging from 0.25 (reduced dust flux) up to 5 (enhanced dust flux). A final simulation was conducted using an atmospheric model estimate of Fe supply during the Last Glacial Maximum, in which the distribution of dust deposition is changed and its global integral is ~3.7 times larger than the modern estimate (9). These experiments were conducted in both model configurations, with specified and prognostic denitrification, to illustrate both the direct effect of Fe in isolation (specified denitrification) and the complete N cycle response (prognostic denitrification). Each simulation was integrated until a new steady state was reached in the oceanic N budget (imbalance <1 TgN/y).

2. Observational Constraints. To determine the most likely degree of Fe limitation of N_2 fixation in the ocean, we compared our model predictions to a variety of geochemical quantities that are strongly influenced by N_2 fixation. Geochemical tracers provide the most appropriate metrics to test long-term regulation of N_2 fixation because they integrate its effect over time and space scales much longer than biological rate measurements. The diagnostics we used are relatively insensitive to poorly constrained model parameters (see *Sensitivity testing*), and are therefore robust indicators of the basin scale partition of N_2 fixation.

Pacific N* convergence. The Pacific Ocean receives the lowest Fe inputs of the three major basins, and is subject to the largest removal of fixed N through denitrification. The degree to which N_2 fixation is able to compensate N losses within the Pacific is therefore a good indicator for the strength of Fe limitation at the basin scale. The basin-wide difference between N_2 fixation and denitrification must be balanced at steady state by an export of N deficits via ocean circulation, and so can be inferred from the net transport convergence of N* into the basin (12). We placed an observational constraint on this quantity by computing the transport of observed N* in both directions across the gateways separating the Pacific from other ocean basins, which amounts to a series of matrix–vector multiplications using the Transport Matrix Method (2). Potential uncertainties in this calculation arise from three factors: (*i*) the nutrient data themselves; (*ii*) the model circulation fields; and (*iii*) the precise geographic definition of the Pacific Ocean, which becomes important only if there is a strong N* gradient across the boundary regions. We used a Monte Carlo approach to account for these uncertainties, repeating the transport calculation while probing a predefined "parameter space" for these three factors. Each iteration selects randomly from a set of three transport operators, randomly defines each Pacific Ocean gateway from a given latitude/longitude range, and produces a "realization" of the N* field by adding spatially correlated noise to the observations.

Transport operators used in this calculation include (*i*) a higher-resolution (2° × 2°) version of the observationally constrained OGCM used in our ecosystem simulations (1), (*ii*) a variation on this model that uses CFC-11 concentrations as an additional constraint on circulation (5), and (*iii*) annual mean circulation fields from the 1° × 1° observationally constrained Estimating the Circulation and Climate of the Ocean (ECCO) project model (2). Pacific Ocean gateways are defined as follows:

Indonesian Throughflow: A meridional transect between Australian and East Asian continents, varied between 113°E and 117°E.

ACC, south of Australia: A meridional transect between Australian and Antarctic continents, varied between 125°E and 130°E.

Drake Passage: A meridional transect between South American and Antarctic continents, varied between 68°W and 72°W.

Bering Straight: A zonal transect between Eurasian and North American continents, varied between 64°N and 68°N.

Nutrient data realizations are constructed following the method described in ref. 1. Briefly, each Monte Carlo simulation generates synthetic nutrient datasets by adding smoothed error fields to the objectively analyzed World Ocean Atlas 2009 (WOA09) climatology. Error fields are derived by taking a random draw from a Gaussian distribution with zero mean and variance estimated from the original dataset. This variance is taken as the sum of a contribution from the raw data (between all observations in a given grid cell, on the WOA09 grid) and a component associated with the objective mapping procedure (the difference between mapped data and raw data, averaged over each depth level). Error fields are then smoothed over a correlation length scale of 200 km by solving a diffusion equation on the original data grid, and are finally interpolated onto the model grid.

The Monte Carlo procedure was repeated 10,000 times to produce a probability density function (PDF) for net Pacific N* convergence, although the PDF had converged after <5000 iterations. The observational constraint presented on Fig. 2*A* represents the mean and SD across all 10,000 calculations, incorporating all three transport models. Results are separated between the models in Fig. S4.

Nutrient tracers. The nutrient stoichiometry of the North Pacific and North Atlantic Subtropical Gyres (NPSG and NASG) exhibit well-known differences easily detected in climatological observations. The NPSG is downstream of an upwelling zone where strongly denitrified waters surface, but receives low Fe inputs, whereas NASG is distant from regions of shallow denitrification but receives the largest Fe inputs of any ocean basin. N_2 fixation therefore transitions from NPSG and into NASG as Fe limitation strengthens in our simulations, producing systematic changes in tracer gradients between those basins that can be compared against the data.

For the two stoichiometric constraints (surface P* and subsurface N*), we define averaging masks for NPSG and NASG (based on observed NO_3 and salinity) to compare simulated tracer distributions to climatological observations from WOA09 (13). NPSG is defined as the oligotrophic North Pacific region where observed [NO_3] falls below 1 μM, and bounded to the North by the 34-psu isohaline, a proxy for the subtropical/subpolar front. NASG is defined as the oligotrophic North Atlantic region with observed [NO_3] < 1 μM, and bounded to the North by the 35.4-psu isohaline (Fig. S5*A*). Within these regions, simulated and observed P* is averaged over the top 75 m (Fig. S5*B*), where primary production occurs in our model, and N* is averaged across the depth of the North Atlantic N* maximum (400–600 m), which is interpreted as a signature of N_2 fixation in that basin (Fig. S5*C*). Our results are not strongly sensitive to variations in the definitions of these averaging regions. We place error estimates on observed P^*_{NPSG}, P^*_{NASG}, N^*_{NPSG}, and N^*_{NASG} by calculating these quantities for each month in the WOA09 monthly climatology and taking the SD. These errors are then propagated into the calculation of interbasin differences, ΔP* and ΔN*.

The difference between ΔP* in regimes 1 and 2 of model (order 0.1 μM) is close to the measurement uncertainty of traditional nutrient data incorporated into the World Ocean Atlas climatology. To aid in the distinction between those regimes, we also examined the P* difference between the sites of the Hawaii Ocean Timeseries (HOT) and Bermuda Atlantic Time Series (BATS) sites, which are considered representative of NPSG and NASG, respectively. At these locations, nutrient observations have been collected for more than 20 y, using high-precision methods. These data were interpolated to standard depths and time intervals and averaged over the top 75 m. The mean and SD

from each time series were then used to characterize the interbasin difference, and its associated uncertainty, which was then compared with model grid cells at corresponding locations.

N isotopes. No climatological dataset exists for $\delta^{15}NO_3$, so we use observations from individual studies at representative locations for the subtropical gyres. We use data from ref. 14 from the HOT site in the central NPSG, and data from refs. 15 and 16 collected along transects in the Sargasso Sea close to the BATS site in NASG (Fig. S5*A*). These data are averaged over the shallow subsurface depth interval between 100 and 300 m and reported with the SEM (Fig. S5*D*). Waters in this depth range should collect the isotopic signature of N_2 fixation while minimizing the influence of water column denitrification in the Pacific, which has a strong isotopic fractionation effect. Simulated $\delta^{15}NO_3$ is averaged from grid cells traversed by the Bermuda transect in NASG, and from the grid cell containing the HOT site and its eight lateral neighbors in NPSG. Simulated and observed $\delta^{15}NO_3$ are compared as interbasin differences, defined as $\Delta\delta^{15}N = \Delta\delta^{15}N_{HOT} - \Delta\delta^{15}N_{BATS}$.

Due to data paucity, we consider this isotopic constraint to be weaker than others used to constrain large-scale N_2 fixation, and thus discuss the results in Fig. S6*A*, rather than the main text.

Suboxic zones. The interbasin distribution of water column denitrification (W) is quantified as the fraction of total global W that occurs in the Pacific (W_{Pac}). It is calculated by integrating volumetric rates across the Pacific, and dividing by the global integral. This is then compared with the same diagnostic from an inverse model, in which denitrification rates were determined from several datasets, including excess N_2 gas (5).

3. Sensitivity testing. We tested the sensitivity of our primary results to features of the model that might affect the distribution of N_2 fixation and the tracer constraints we use. Specifically, we wish to ensure that the appearance of three distinct Fe limitation regimes is robust, and that observations are always most consistent with the second regime, in which Fe controls the distribution of N_2 fixation within ocean basins, but not between them.

Variable R_O. For simplicity, we assumed a constant N:P requirement (R_O) of 16:1 in non N_2-fixing plankton in our primary simulations. However, N:P uptake ratios vary between marine biomes according to the dominant plankton taxa (17, 18), and these variations are important in regulating the NO_3 content of the ocean as a whole (3). We tested the sensitivity of our results to large-scale variations in R_O by repeating our simulations using the parameterization of ref. 3, where community N:P is linked to the relative abundance of diatoms as gleaned from the silicic acid distribution. The competition between diazotrophs and high N:P plankton in this configuration raises the ocean's N reservoir, increasing global mean NO_3 and N*, and reducing mean P*.

However, variable R_O has little effect on the changing patterns of N_2 fixation and accompanying tracer patterns produced by strengthening Fe limitation. N_2 fixation transitions out of the eastern Pacific and then the Pacific Ocean as a whole at similar values of Q_F/Q_O to our default simulations, and ΔP^* and ΔN^* exhibit similar trends, increasing gradually in regime 2 and sharply in regime 3 (Fig. S7 *A–D*). These interbasin tracer differences thus provide robust constraints on the large-scale distribution of N_2 fixation, that are independent of factors controlling their mean concentrations. Simulations with variable R_O again reach best agreement with observed ΔP^* and ΔN^* constraints within the intermediate regime of Fe limitation, in which Fe controls N_2 fixation locally, but not at the basin scale.

Growth rate handicap. In our default simulations, we assumed the intrinsic energetic expenditure associated with N_2 fixation (represented by a reduced maximum growth rate) to be relatively low, taking $\mu_F/\mu_O = 0.9$. Therefore, the total competitive handicap faced by diazotrophs in our model is mostly associated with their heightened Fe requirements (at least when $Q_F/Q_O > 1$). We tested whether a stronger "intrinsic" handicap would affect our results by repeating our experiments but taking $\mu_F/\mu_O = 0.7$ (Fig. S7 *E–H*). Their reduced growth rate made it easier for Fe limitation to exclude diazotrophs from regions with low dust deposition when their Fe requirements were raised, causing transitions between Fe limitation regimes to occur at lower values of Q_F/Q_O. The interbasin shift of N_2 fixation from the Pacific toward the Indian and Atlantic oceans now commences at Q_F/Q_O between 10 and 20, rather than at ~25 in our default simulations. However, the range of Q_F/Q_O in which model is consistent with observed ΔP^* and ΔN^* is also shifted correspondingly lower. In other words, even though the Fe limitation regimes have been shifted with respect to Q_F/Q_O, observations still support the regime of intermediate Fe limitation in which denitrification and N_2 fixation remain coupled at the basin scale.

Simplified Fe limitation scheme. Because this study aims to constrain the net influence of Fe on N_2 fixation, and not specific Fe-cycle processes or parameters, our main conclusions are independent of the exact treatment of the Fe cycle. To demonstrate this, we conducted a series of experiments that used the much simpler parameterization of diazotroph Fe limitation used by refs. 3 and 19). Instead of explicitly simulating dissolved Fe, the Fe dependence of diazotroph growth is represented by scaling their maximum growth rate by the distribution of dust deposition onto the surface ocean. The scaled maximum growth rate (μ'_F) is given by:

$$\mu'_F = \mu_F \frac{J_{dust}}{J_{dust} + K_{dust}},$$

where J_{dust} is the dust flux from the atmosphere and K_{dust} is constant that determines the strength of this scaling, i.e., determines the degree to which μ'_F varies between regions of high and low dust deposition. Raising K_{dust} in this configuration is therefore the equivalent of raising Q_F/Q_O in the explicit Fe-cycle mode, and the three familiar regimes of Fe limitation arise as before (Fig. S8 *A–D*). With K_{dust} between 0 and 0.02 g m^{-2} y^{-1}, the interbasin spread of N_2 fixation mirrors that of denitrification with ~60% occurring in the Pacific, and the majority found close to the Eastern upwelling zones (regime 1). Between $0.02 < K_{dust} < 0.2$ g m^{-2} y^{-1}, N_2 fixation shifts toward the western Pacific (regime 2), and at higher values, it shifts out of the Pacific and into the dustier basins (regime 3). Within these regimes, simulated ΔP^* and ΔN^* exhibit similar behavior to their counterparts in the explicit Fe-cycle model, and once again their comparison with observations supports the intermediate Fe limitation regime, in which denitrification and N_2 fixation are coupled at the basin scale. These results suggest that any representation of Fe limitation that captures the asymmetry in Fe supply between basins will lead to the same conclusions reached in this study.

Benthic Fe sources. Our default simulations assumed that bioavailable Fe enters the ocean only via atmospheric dust deposition. It is therefore unsurprising that raising the diazotrophic requirement for Fe shifts N_2 fixation out of the Pacific Ocean and toward regions of enhanced dust supply. However, recent studies have highlighted the importance of seafloor sediments as an additional source of Fe. To test the sensitivity of our results to this additional source, we extended our model to include benthic Fe release, parameterizing it as in ref. 20:

$$J_{ben}\mathrm{Fe} = r_{Fe:C} C_{ox},$$

where C_{ox} is the degradation rate of organic carbon in the seafloor sediments, and the ratio of Fe release to carbon degradation ($r_{Fe:C}$) is specified to hold the globally integrated benthic

flux equal to the integrated atmospheric deposition rate. We found that this additional Fe source had little bearing on our results. The atmospheric source, supplied directly to the surface euphotic zone is therefore more important in fueling N_2 fixation than Fe released from sediments, which may be subject to scavenging before reaching diazotrophic habitats. However, in some regions, the additional Fe source can fuel additional N_2 fixation, over that supported by dust deposition, making diazotrophs less susceptible to Fe limitation. This causes transitions between Fe limitation regimes to occur at slightly higher values of Q_F/Q_O than in default simulations, with the shift to basin-scale Fe limitation (and an imbalanced Pacific N budget) occurring only at Q_F/Q_O ~30, rather than ~25 in the default model (Fig. S8 *E* and *F*). However, in these simulations, our geochemical constraints allow for a correspondingly higher range of Q_F/Q_O (Fig. S8 *G* and *H*), again supporting an intermediate degree of Fe limitation.

Taken together, these sensitivity tests demonstrate that the geochemical quantities we evaluate allow us to constrain the large-scale distribution of N_2 fixation and the environmental factors that control it, rather than simply constraining a value of the biological parameter Q_F/Q_O. They require a degree of Fe control that limits local but not basin-scale N_2 fixation rates, regardless of the exact values of Q_F/Q_O at which that occurs.

1. DeVries T, Primeau F (2011) Dynamically and observationally constrained estimates of water-mass distributions and ages in the global ocean. *J Phys Oceanogr* 41(12): 2381–2401.
2. Khatiwala S (2007) A computational framework for simulation of biogeochemical tracers in the ocean. *Global Biogeochem Cycles* 21(3):GB3001, 10.1029/2007GB002923.
3. Weber T, Deutsch C (2012) Oceanic nitrogen reservoir regulated by plankton diversity and ocean circulation. *Nature* 489(7416):419–422.
4. Luo Y-W, et al. (2012) Database of diazotrophs in global ocean: Abundances, biomass and nitrogen fixation rates. *Earth System Science Data* 5(1):47–73.
5. DeVries T, Deutsch C, Primeau F, Chang B, Devol A (2012) Global rates of water-column denitrification derived from nitrogen gas measurements. *Nat Geosci* 5(8):547–550.
6. Middelburg JJ, Soetaert K, Herman PMJ, Heip CHR (1996) Denitrification in marine sediments: A model study. *Global Biogeochem Cycles* 10(4):661–673.
7. DeVries T, Deutsch C, Rafter PA, Primeau F (2012) Marine denitrification rates determined from a global 3-dimensional inverse model. *Biogeosciences Discuss* 9(10):14013–14052.
8. Parekh P, Follows MJ, Boyle EA (2005) Decoupling of iron and phosphate in the global ocean. *Global Biogeochem Cycles* 19(2):GB2020, 10.1029/2004GB002280.
9. Mahowald NM, et al. (2006) Change in atmospheric mineral aerosols in response to climate: Last glacial period, preindustrial, modern, and doubled carbon dioxide climates. *J Geophys Res* 111(D10):D10202, 10.1029/2005JD006653.
10. Follows MJ, Dutkiewicz S, Grant S, Chisholm SW (2007) Emergent biogeography of microbial communities in a model ocean. *Science* 315(5820):1843–1846.
11. Gruber N, Sarmiento JL (1997) Global patterns of marine nitrogen fixation and denitrification. *Global Biogeochem Cycles* 11(2):235–266.
12. Deutsch C, Gruber N, Key RM, Sarmiento JL, Ganaschaud A (2001) Denitrification and N_2 fixation in the Pacific Ocean. *Global Biogeochem Cycles* 15(2):483–506.
13. Garcia H, Locarnini R, Boyer T, Antonov J (2010) *World Ocean Atlas 2009: Nutrients (Phosphate, Nitrate, Silicate), (NOAA Atlas NESDIS)* (US Gov. Print. Off, Washington, DC), Vol 4.
14. Sigman DM, DiFiore PJ, Hain MP, Deutsch C, Karl DM (2009) Sinking organic matter spreads the nitrogen isotope signal of pelagic denitrification in the North Pacific. *Geophys Res Lett* 36(8):L08605, 10.1029/2008GL035784.
15. Knapp AN, DiFiore PJ, Deutsch C, Sigman DM, Lipschultz F (2008) Nitrate isotopic composition between Bermuda and Puerto Rico: Implications for N_2 fixation in the Atlantic Ocean. *Global Biogeochem Cycles* 22(3):GB3014, 10.1029/2007GB003107.
16. Knapp AN, Sigman DM, Lipschultz F (2005) N isotopic composition of dissolved organic nitrogen and nitrate at the Bermuda Atlantic Time-series Study site. *Global Biogeochem Cycles* 19(1):GB1018, 10.1029/2004GB002320.
17. Weber TS, Deutsch C (2010) Ocean nutrient ratios governed by plankton biogeography. *Nature* 467(7315):550–554.
18. Martiny AC, et al. (2013) Strong latitudinal patterns in the elemental ratios of marine plankton and organic matter. *Nat Geosci* 6(4):279–283.
19. Somes CJ, Schmittner A, Altabet MA (2010) Nitrogen isotope simulations show the importance of atmospheric iron deposition for nitrogen fixation across the Pacific Ocean. *Geophys Res Lett* 37(23):L23605, 10.1029/2010GL044537.
20. Moore J, Braucher O (2008) Sedimentary and mineral dust sources of dissolved iron to the world ocean. *Biogeosciences* 5(3):631–656.

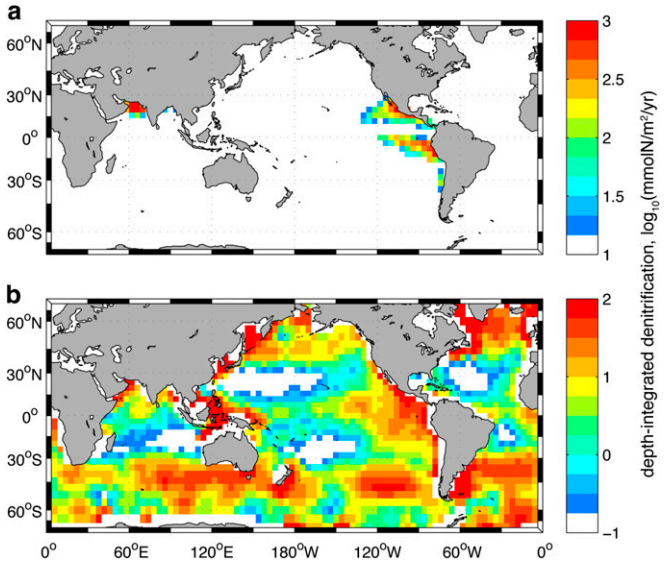

Fig. S1. Model denitrification rates integrated over depth. (*A*) Water-column denitrification is distributed between the eastern tropical North and South Pacific (25 TgN/y) and the Arabian Sea (15 TgN/y) based on the inverse results of ref. 5. (*B*) Benthic denitrification is distributed based on the flux of organic matter to the seafloor, but is scaled to maintain a specified global rate, here 140 TgN/y.

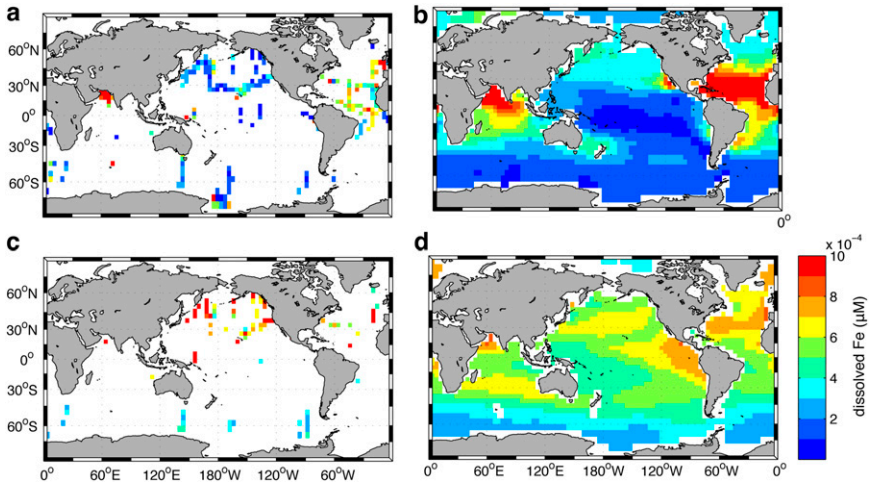

Fig. S2. Dissolved Fe (free + complexed) distribution in surface (*A* and *B*) and intermediate (*C* and *D*) waters from observations (*A* and *C*) and simulations with $Q_F/Q_O = 20$ (*B* and *D*). (*A*) Observed surface dissolved Fe largely mirrors the distribution of mineral dust deposition, with the highest concentrations in the tropical Atlantic and Indian Ocean. (*B*) Simulated surface Fe reproduces these interbasin variations. (*C*) The dominant pattern observed in intermediate waters (800–1000 m) is a northward increase in all basins, with lowest values in the Southern Ocean. (*D*) Again, this pattern is well reproduced in the model, although simulated concentrations in the North Pacific are somewhat low, possibly due to a missing source of Fe released from sediments.

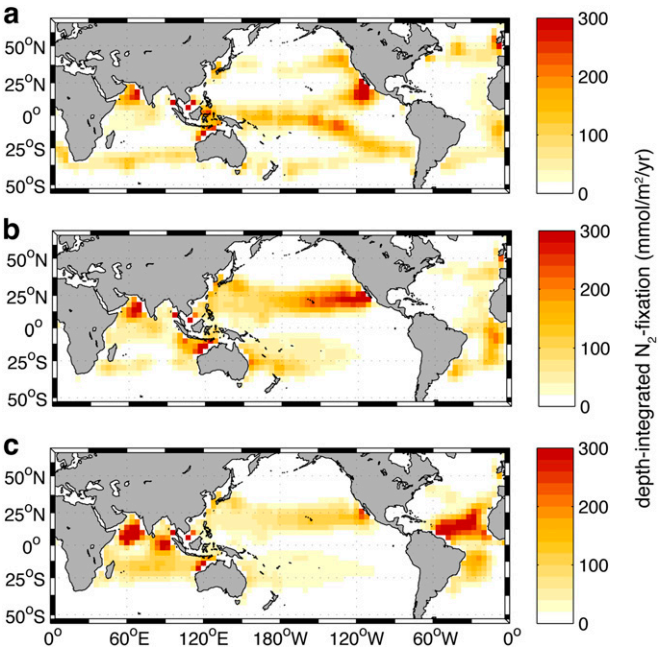

Fig. S3. Distributions of N_2 fixation under the three Fe limitation regimes. (*A*) Regime 1 ($Q_F/Q_O = 1$), in which the large-scale distribution of N_2 fixation closely mirrors that of denitrification, and concentrates toward upwelling zones where N-deficient waters reach the surface. (*B*) Regime 2 ($Q_F/Q_O = 20$), in which N_2 fixation becomes more separated from the eastern denitrification zones in the Pacific Ocean but its interbasin spread remains unchanged from regime 1. (*C*) Regime 3 ($Q_F/Q_O = 50$), in which Fe limitation reduces N_2 fixation within the Pacific Ocean as a whole, and its interbasin distribution begins to mirror that of the atmospheric Fe source.

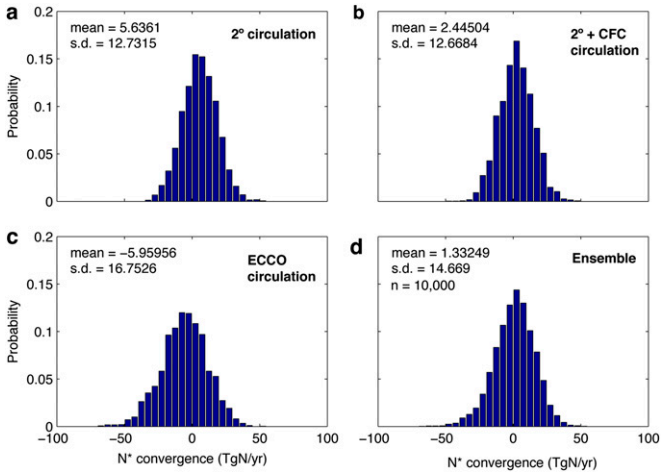

Fig. S4. Probability density functions for transport convergence of observed N* into the Pacific Ocean, calculated in three circulation models with errors propagated from the nutrient data. PDFs are shown for individual circulation models: (*A*) 2° observationally constrained circulation model; (*B*) a second configuration of the 2° model with added CFC-11 constraint; and (*C*) annual mean circulation from the ECCO project model. (*D*) PDF from the ensemble of three models, from which the range reported in Fig. 2*A* is derived.

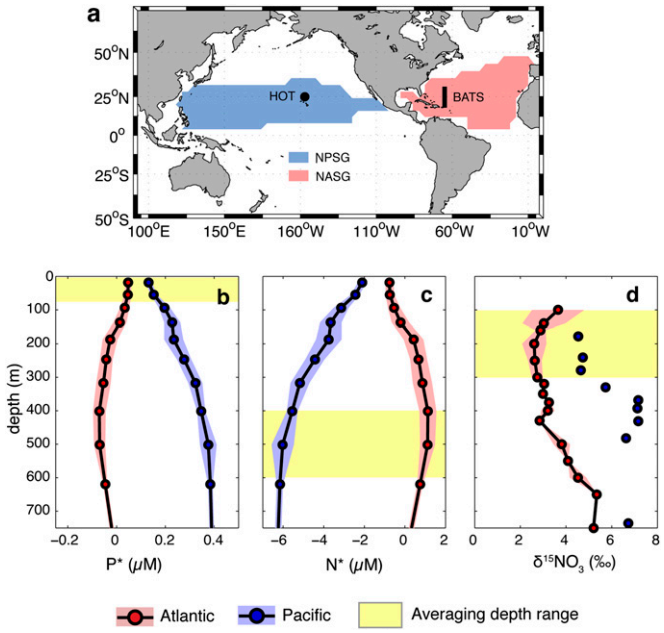

Fig. S5. Observational constraints on Fe limitation regimes. (*A*) Locations for comparison between simulations and observations. Simulated and observed climatological P* and N* are averaged across the shaded regions, representing the North Pacific (blue) and North Atlantic (red) subtropical gyres, to compute the interbasin tracer gradients we use as constraints. For $\delta^{15}NO_3$, these gradients are computed from individual localities—the HOT site in NPSG (black dot) and the Bermuda transect proximal to the BATS site in NASG (black line). (*B*) P* profiles for NPSG and NASG. ΔP^* ($P^*_{NPSG} - P^*_{NASG}$) is calculated in surface waters (0–75 m), where nutrient uptake occurs in our model. (*C*) N* profiles for NPSG and NASG. ΔN^* ($N^*_{NASG} - N^*_{NPSG}$) is calculated across the depth of the prominent N* maximum in the Atlantic Ocean (400–600 m). (*D*) $\delta^{15}NO_3$ profiles from HOT and BATS. $\Delta\delta^{15}NO_3$ is calculated in shallow subsurface waters (100–300 m), which accumulate the isotopic signature of N_2 fixation.

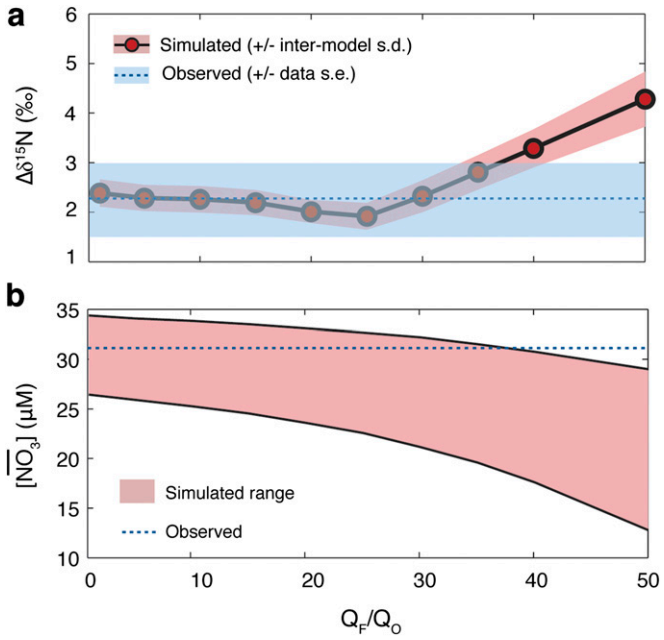

Fig. S6. Additional constraints on Fe limitation of N_2 fixation. (*A*) $\Delta\delta^{15}N$ quantifies the isotopic difference between shallow subsurface waters in the North Pacific and North Atlantic subtropical gyres, based on the representative HOT and BATS locations ($\Delta\delta^{15}N_{HOT} - \Delta\delta^{15}N_{BATS}$). Simulated values and error envelopes represent mean and SD from four benthic denitrification scenarios. In regime 1, Pacific NO_3 is slightly isotopically heavier, due to the influence of recently denitrified waters transported from the eastern margin. In regime 2, the difference between the two basins is gradually reduced, as N_2 fixation shifts westward toward the HOT site in the Pacific, introducing light NO_3 that counteracts the denitrification signature. In regime 3, the isotopic difference increases sharply, as N_2 fixation and the associated influx of light NO_3 transition out of the Pacific and toward the Atlantic. The data constraint is derived from the mean and SE of observations from individual studies at the two sites, rather than climatological data. Due to the paucity of data, the observed value is subject to large uncertainty and is thus a weak constraint on Q_F/Q_O, excluding only the most strongly limited cases ($Q_F/Q_O > 40$) in which N_2 fixation is strongly focused in the tropical Atlantic Ocean. (*B*) The mean NO_3 content of seawater varies as a function of Fe limitation regimes, but is also strongly sensitive to other factors that regulate the ocean N reservoir (3). The envelope represents the range obtained between scenarios with strong and weak denitrification, and those with Redfield phytoplankton ($R_O = 16$) and phytoplankton with variable stoichiometry (3). Although mean ocean [NO_3] varies considerably for each Q_F/Q_O, the observed value cannot be reproduced under any circumstances in strongly Fe-limited cases with $Q_F/Q_O > 35$.

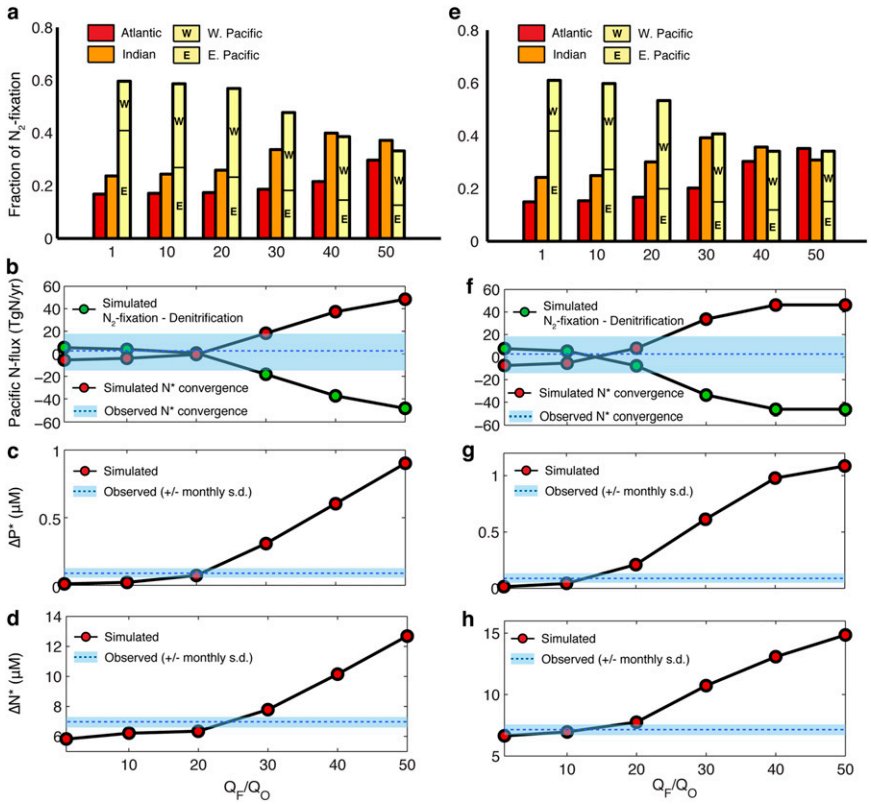

Fig. S7. Sensitivity testing to factors that influence competitive scope of diazotrophs. (*A*–*D*) Variations in nondiazotroph N:P requirements (R_O), which are prescribed following ref. 3; (*E*–*H*) growth rate of diazotrophs compared with other plankton (μ_F/μ_O), which is lowered to 0.7 from default value of 0.9. (*A*) Distribution of N_2 fixation in simulations which account for variations in R_O (compare with Fig. 1*A*). The model reproduces the same large-scale changes observed in our default simulations, at similar values of Q_F/Q_O. (*B*–*D*) The N budget of the Pacific Ocean and predicted tracer distributions are again most consistent with observational constraints when Q_F/Q_O falls between 20 and 25, corresponding to regime 2 (compare with Fig. 2). (*E*) Distribution of N_2 fixation in simulations with $\mu_F/\mu_F = 0.7$ (compare with Fig. 1*A*). As they are now weaker nutrient competitors, diazotrophs become Fe-limited at lower values of Q_F/Q_O, and the transition to basin-scale Fe limitation (regime 3) occurs between $10 < Q_F/Q_O < 20$ (previously at ~25). (*F*–*H*) The range of Q_F/Q_O in which the model can match geochemical constraints shifts to correspondingly lower values (compare with Fig. 2). As such, the observations require that Fe does not limit basin-scale N_2 fixation, regardless of the strength of their intrinsic growth-rate handicap. Note the lack of error bars on simulated values, as only one benthic denitrification rate was tested here.

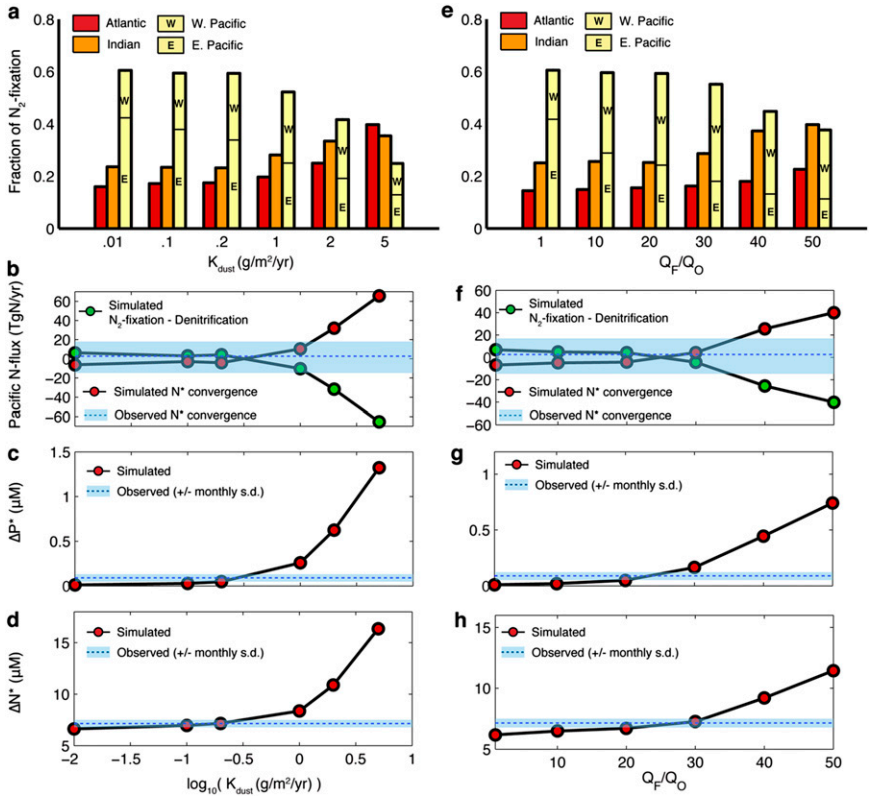

Fig. S8. Sensitivity testing to model representation of the ocean Fe cycle. (*A*–*D*) The model is greatly simplified by replacing the explicit Fe cycle of default simulations with a simpler parameterization that scales diazotroph growth with atmospheric dust fluxes (3, 19); (*E*–*H*) additional complexity is added to the model, by incorporating benthic Fe sources of equal magnitude to atmospheric sources. (*A*) Distribution of N_2 fixation in simulations with simple dust scaling for diazortoph growth (compare with Fig. 1). Strengthening the scaling (i.e., raising K_{dust}) produces the same shifting patterns of N_2 fixation as raising Q_F/Q_O in the explicit model. (*B*–*D*) Geochemical constraints again require an intermediate degree of Fe limitation ($0.1 < K_{dust} < 1$), in which Fe modulates the distribution of N_2 fixation within the Pacific, but not its distribution between basins (compare with Fig. 2). (*E*) Distribution of N_2 fixation in simulations with benthic Fe release (compare with Fig. 1). Our results remain largely unchanged, although the additional source of Fe makes diazotrophs less susceptible to Fe limitation, and the transition to basin-scale Fe limitation occurs at higher values of Q_F/Q_O than in default simulations: The N budget of the Pacific Ocean remains relatively balanced at $Q_F/Q_O = 30$. (*F*–*H*) The range of Q_F/Q_O consistent with observational constraints also shifts to include slightly higher values (compare with Fig. 2), and again requires Fe limitation of N_2 fixation at the local, but not basin, scale.

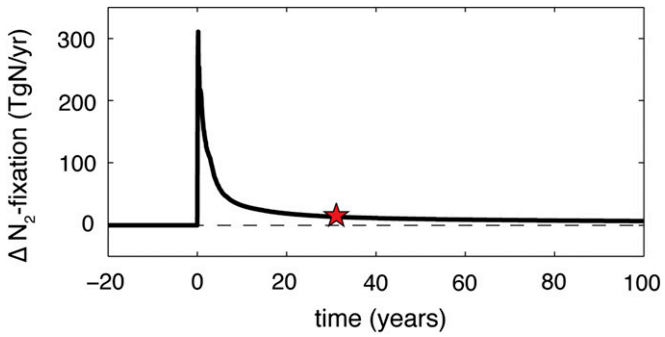

Fig. S9. Timeseries following response of N_2 fixation to basin-wide Fe fertilization in the Pacific (accompanies Fig. 4*B*). Plotted is the Pacific N_2 fixation anomaly: basin-integrated N_2 fixation minus its initial rate from simulation with $Q_F/Q_O = 20$. At time 0, the atmospheric Fe supply is increased by 1 g m^{-2} y^{-1} across the Pacific, and maintained at this rate for the remainder of the simulation. Initially, Fe fertilization stimulates a large increase in N_2 fixation throughout the eastern Pacific, but this reduces the PO_4 supply to the subtropical gyres, suppressing N_2 fixation in those regions (Fig. 4*B*). After just 30 y (red star indicates the time represented in Fig. 4*B*), basin-wide N_2 fixation has returned to within 10 TgN/y of its prefertilization rate.

Table S1. Parameters of the ecosystem/biogeochemical model

Parameter	Definition	Units	Value or range
f_{Fe}	Fraction of Fe in mineral dust	unitless	0.035
α_{Fe}	Soluble fraction of Fe	unitless	0.01
β_{Fe}	Ligand binding strength	$(\mu MFe)^{-1}$	10^5
[L]	Fe-binding ligand concentration	μM	10^{-3}
k_{sc}	Scavenging rate of free Fe	day^{-1}	$1.1*10^{-3}$
Q_O	Fe:P ratio for nondiazotrophs	mmol/mol	0.47
Q_F	Fe:P ratio in diazotrophs	mmol/mol	0.47–23.5
ε_{WC}	Isotopic enrichment factor for water column denitrification	‰	25
ε_B	Isotopic enrichment factor for benthic denitrification	‰	0
ε_F	Isotopic enrichment factor for N_2 fixation	‰	0
ε_{prod}	Isotopic enrichment factor for nitrate assimilation	‰	5
ε_{prod}	Isotopic enrichment factor for remineralization	‰	0
$r_{O:N}$	O_2:N ratio in production/remineralization	unitless	9.3
r_{den}	NO_3 consumption: remineralization ratio in water-column denitrification	unitless	7
ϕ_{DOM}	Fraction of plankton organic matter to DOM	unitless	0.1
τ_{DOM}	Turnover time of DOM	years	1 (1–2 in O_2 simulations)

Other parameters are as in ref. 3.